

Magnetically Levitated Homopolar Hollow-Shaft Motor

Thomas Schneeberger, *Student Member, IEEE*, Thomas Nussbaumer, *Member, IEEE*,
and Johann W. Kolar, *Senior Member, IEEE*

Abstract—This paper describes a novel and compact topology for contactless levitation and rotation of a wide annular rotor through the walls of a sealed process chamber. In the proposed setup, a homopolar magnetic bearing biased by permanent magnets is combined with a high-pole-number segment motor. The paper discusses the functional principle of the motor, and gives design and optimization guidelines for the bearing and the drive unit, respectively. An experimental system is presented along with a set of measurement results verifying the theoretical considerations.

Index Terms—Bearingless motor, hollow-shaft motor, magnetic bearing, sealed chamber.

I. INTRODUCTION

THE REPRODUCIBILITY of many industrial processes can be improved by the use of hermetically sealed process chambers, since they facilitate proper control of crucial process parameters such as pressure, temperature, or composition of the gas or liquid, which is surrounding the object that is to be processed. These chambers are used in biotechnological and pharmaceutical applications as well as in the semiconductor industry, where they also prevent leakage of potentially harmful chemicals into the environment. State-of-the-art wafer production requires a device placed inside the sealed chamber that rotates the wafer during processing, thereby providing a uniformly distributed concentration and flow pattern [1]. The design of existing process chambers for wafer production relies on a gastight feed through of the rotating drive axis (through the bottom of the process chamber), and is therefore afflicted with two major disadvantages. Not only are the drive shaft, the shaft sealing, the bearings, and the motor rather bulky, sometimes occupying a significant portion of the space available inside the chamber, but they also generate particles, which are detrimental for the media inside the chamber, at every frictional contact between moving parts.

In this paper, a novel bearingless hollow-shaft motor, which is generally based on the principle of the “bearingless motor” [3]–[11], is described. This motor allows for contactless levitation and rotation effectuated through the walls of the chamber

on a rotor, to which a clamping device carrying the process object is attached (Fig. 1). Due to the integration of the drive and the magnetic bearing, a very compact setup is achieved and a very little space is needed for the motor. All elements necessary for the drive and bearing (coils, sensors, and electronics) are placed outside the chamber and are integrated in the motor stator. Also, the corresponding power and data processing electronics can be placed outside the process chamber, and are therefore not exposed to harmful process chemicals and can be replaced quickly in the case of a failure. The object to be treated is clamped in the middle of an annular rotor, and the whole place in the chamber above and beneath the object remains free from any bearing or drive elements. Therefore, process sources, such as nozzles or radiation sources, can be placed on both sides of the object, which allows a simultaneous treatment of both object surfaces.

In contrary to the conventional bearingless motor, the new concept proposed in this paper features a homopolar bearing, which means that the bearing forces can be applied in the stationary frame, and ideally no rotational-speed-dependent instabilities and/or limitations occur [12]. This is a crucial advantage for the accurate control of the radial displacement of the rotor over a wide rotational speed range, since already small radial movements of the process object can significantly impair the process quality. Moreover, the conventional bearingless motor featuring a multipolar bearing would lead to an excessive number of stator claws for large rotor diameters as for the case at hand, and therefore, to a very large stator setup [4], [5].

The paper is structured as follows. In Section II, the basic principle of the proposed motor topology is explained. Guidelines for the design of the homopolar bearing are given in Section III. Subsequently, the design of the multipolar drive and the optimization regarding minimum acceleration time are carried out in Section IV. Finally, in Section V, the performance of the new topology is proven for a prototype of the system.

II. MOTOR FUNCTIONAL PRINCIPLE

In principle, the rotor has 6 spatial DOF: linear motion and rotation along with each of the three axes in an xyz -system. While the rotor is held in place by the bearing, all three of its translatory modes and two of its rotatory modes of motion must be suppressed. The only remaining degree of freedom is the desired rotation around the z -axis.

In contrast to conventional magnetically levitated drives, the bearing forces in a “bearingless motor” are not built up in additional magnetic bearings placed along the axis of rotation, but in the motor itself: the active motor part generates the torque as

Manuscript received July 27, 2008; revised January 17, 2009. First published May 15, 2009; current version published November 18, 2009. Recommended by Technical Editor M. Benbouzid.

T. Schneeberger is with Levitronix GmbH, CH-8005 Zürich, Switzerland (e-mail: schneeberger@levitronix.com).

T. Nussbaumer is with Levitronix GmbH, CH-8005 Zürich, Switzerland (e-mail: nussbaumer@levitronix.com).

J. W. Kolar is with the Power Electronic Systems Laboratory, Swiss Federal Institute of Technology Zürich, CH-8092 Zürich, Switzerland (e-mail: kolar@lem.ee.ethz.ch).

Digital Object Identifier 10.1109/TMECH.2009.2018836

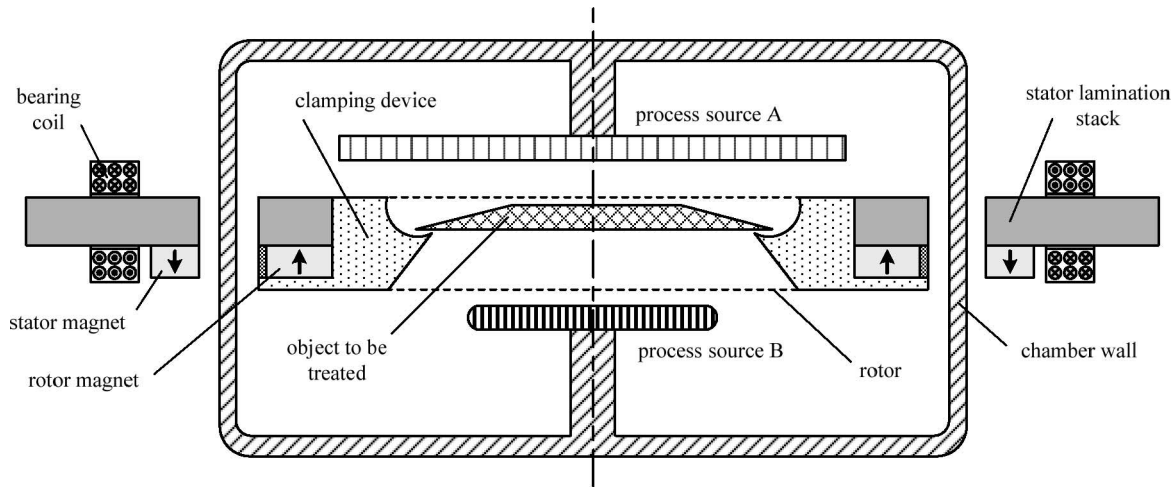


Fig. 1. Arrangement of a hermetically sealed process chamber with the proposed bearingless hollow-shaft drive and two process sources. All electric parts of the system are placed outside the chamber, whereas the rotor floats inside the process chamber and is levitated by magnetic fields through the chamber walls. Therefore, the rotor is easily accessible from both sides allowing for simultaneous treatment of both object surfaces.

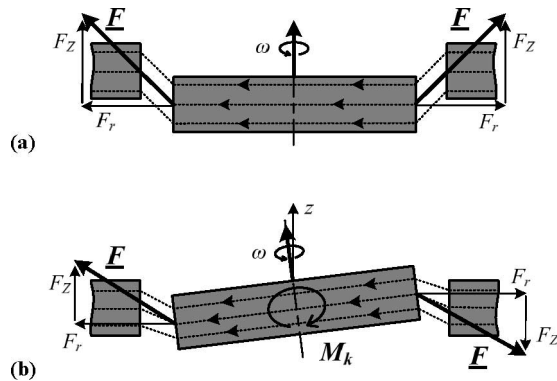


Fig. 2. (a) Axial support and (b) stabilization against tilting of the rotor by passive magnetic forces in a "bearingless motor" [3], [11].

well as radial magnetic bearing forces. Because the length of the rotor is small compared to its diameter, it is possible to stabilize 3 spatial DOF (z -position, tilting moment in x - and y -direction) passively by attractive magnetic forces (minimization of reluctance, Fig. 2), so that only one active radial bearing (for x - and y -position) is needed [13]. Although being stabilized only passively, the axial position of the rotor lies within a narrow range for small loads.

Fig. 3 shows the functional principle of the homopolar active radial bearing. Permanent magnets placed on the rotor and on the stator provide a bias flux in the air gap. Depending on the axial position of the rotor, the bearing windings are supplied with a current, which alters the flux density in the air gap, thereby generating a resulting Maxwell force toward the target position. In order to maximize this Maxwell force, both opposite bearing windings are connected against each other. Fig. 4 shows the magnetic flux density distribution in two opposite bearing air gaps for an exemplary bearing current. With the shown current feed, the magnetic flux density of the premagnetization is increased in the left-side air gap and reduced in the right-side air

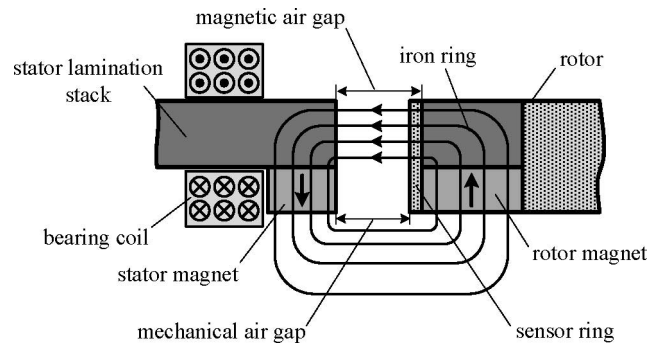


Fig. 3. Homopolar passive magnetic bearing to support the axial rotor position and active radial bearing to control the radial rotor deflection. The bearing is biased by rare earth permanent magnets, which reduces the size of the bearing coil.

gap, and the resulting force is generated, which moves the rotor toward the left direction.

The appropriate reference bearing current is calculated by a PID position controller and adjusted by a subordinate current controller. The rotor position is measured by at least two displacement sensors, which are faced toward the sensor ring of the rotor (see rotor construction in Fig. 3). The concentricity and surface quality of this ring are of high importance for the suspension quality, since asymmetries will automatically lead to unbalances, and consequently, to vibrations for higher rotation speeds. In the same manner, mass unbalances and magnetic asymmetries may also cause similar problems. Even though unbalance compensation schemes may be employed in the control scheme, any kind of asymmetry should be avoided wherever possible in the manufacturing process.

The use of high-energy permanent magnets to generate a magnetically biased bearing flux leads to a compact system: the neodymium iron boron magnets used in this setup have coercive field strengths of more than 1000 kA/m. As an example, a coil with 8000 A turns generates the same field strength as a magnet

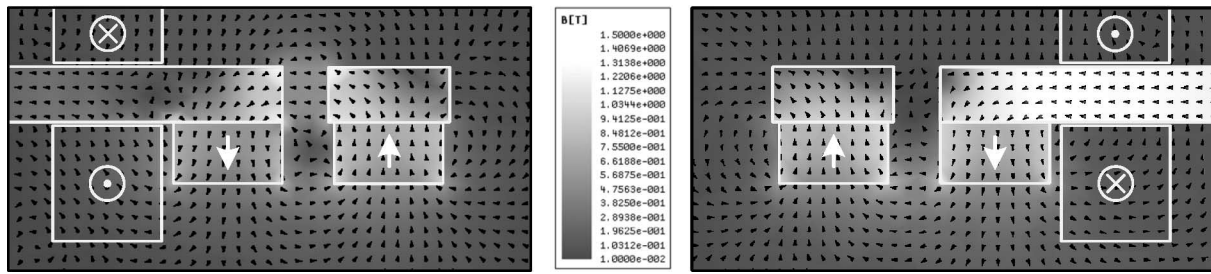


Fig. 4. Magnitude and orientation of the magnetic flux density distribution for a bearing current of 2300 A turns in two opposite bearing windings. With this current feed, the magnetic flux density is increased in the left air gap and reduced in the right air gap, which causes a resulting force on the rotor toward the left side.

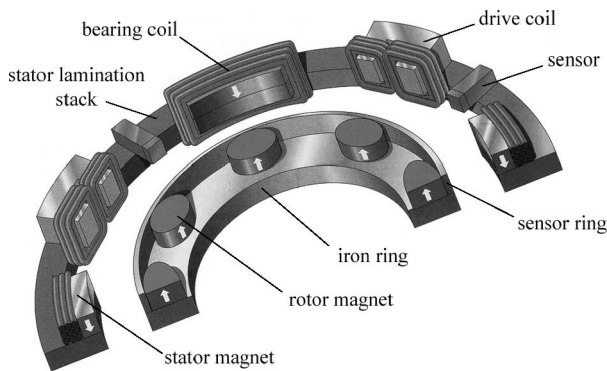


Fig. 5. 3-D sectional view of the hollow-shaft motor. Here, independently of the rotor angle, one rotor pole always lies in front of one stator pole. In this setup, two drive coils are provided for one drive phase.

with a height of only 8 mm. Furthermore, a reasonable control bearing force on the rotor is obtainable with moderate bearing currents due to the biasing of the bearing flux by the permanent magnets together with the square dependence of the Maxwell force on the magnetic flux density [15].

In order to simultaneously provide an alternating field for the drive and maintain the homopolar bearing characteristic, the rotor magnets are placed in pole distance and with equal direction of polarization (Fig. 5). Therefore, they generate a high-pole, modulated but rectified bias flux. In order to keep the bearing force independently of the rotor angle, and thus, constant during rotation, the width of the bearing stator claws are advantageously matched to a multiple of the pole pair width of the rotor.

This rotor magnet flux in interaction with the drive segments on the stator serves for the generation of the torque according to the principle of a synchronous rotating field machine, as will be discussed in Section IV. Thus, the rotor magnets are used to generate both drive and bearing forces, while on the stator separate coils are used for the drive and bearing. This results on the one hand in a very compact (and lightweight) rotor construction, and on the other hand in separate bearing and drive units at the stator, where coupling among each other can be neglected and the design can be carried out separately.

For the field-orientated speed control, two hall sensors—placed on the stator—determine the rotor angle in a sine–cosine

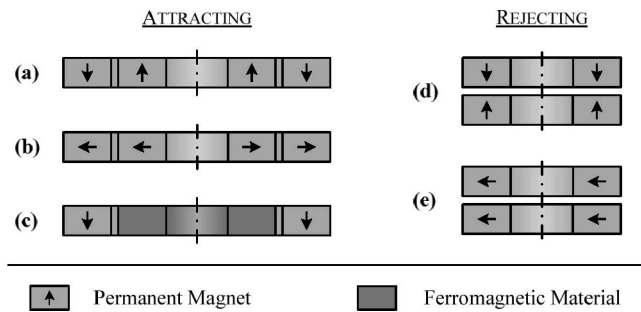


Fig. 6. Arrangements of passive homopolar axial magnetic bearings [12].

analysis. For a detailed information on the current and position control procedure, see [9] and [16] for the sake of brevity.

III. BEARING DESIGN ASPECTS

Due to the necessity of exact radial positioning of the process object and the required high compactness of the system, a homopolar bearing setup with active radial stabilization and passive axial support is preferably selected. This implicates that the axial deflection and the tilting of the rotor are passively stabilized through reluctance forces in the air gap (cf., Fig. 2). Fig. 6 shows some basic arrangements of passive axial magnetic bearings, which can be divided into configurations with attracting magnetic forces and with rejecting forces (more configurations are described in [12]). As Fig. 6 indicates a passive axial bearing based on rejecting forces [Fig. 6(d) and (e)], it leads to a vertical construction, which is not desirable for the application at hand (cf., Fig. 1). Attractive forces can be either built up by interaction of permanent magnets [Fig. 6(a) and (b)] or by interaction of permanent magnets with ferromagnetic material, such as iron [Fig. 6(c)]. However, the latter typically has significantly lower stabilizing axial stiffness compared to setups based on permanent magnet interaction. Furthermore, the use of high energy density permanent magnets both on the rotor and on the stator side leads to very compact setups.

Compared to the configuration in Fig. 6(a), the configuration in Fig. 6(b) allows for a higher motor torque due to smaller leakage flux. However, the configuration in Fig. 6(a) provides a higher axial stiffness as well as a significantly higher force–current factor, and therefore, seems to be advantageous for this application (see Table I). The importance of these parameters

TABLE I
COMPARISON OF THE CRUCIAL BEARING PARAMETERS (3-D FEM SIMULATION RESULTS) FOR A CONFIGURATION WITH AXIALLY MAGNETIZED PERMANENT MAGNETS AND RADIALLY MAGNETIZED MAGNETS FOR A MAGNET HEIGHT OF 8 mm AND DIFFERENT AIR-GAP LENGTHS δ

Gap δ [mm]	Axial stiffness k_z			Radial stiffness k_r			Force-Current Factor k_f		
	Axial Mag. [N/mm]	Radial Mag. [N/mm]	Δ [%]	Axial Mag. [N/mm]	Radial Mag. [N/mm]	Δ [%]	Axial Mag. [mN/Atturns]	Radial Mag. [mN/Atturns]	Δ [%]
3	95.8	89.9	6.6	168.7	101.1	66.8	241.9	37.0	654
6	45.5	38.8	17.2	44.8	31.1	44.1	71.8	17.1	420
9	25.3	19.2	31.8	20.0	13.4	49.3	28.7	17.4	165

will be discussed in the following. The addition of ferromagnetic material, which is required for the radial control flux, leads finally to the construction shown in Fig. 3. As already mentioned in the previous section, in this setup the permanent magnets not only provide axial support but also serve for the biasing of the active radial bearing, which leads to a very compact design.

In the following, the crucial parameters in the bearing design will be explained and guidelines will be given.

First, the axial stiffness k_z (newton per millimeter) describes the force (newton), which has to be employed to move the rotor 1 mm axially out of its stable position. Generally, a high axial stiffness is desired to avoid an appreciable deflection of the rotor due to its weight. For a given maximum allowed axial displacement Δz_{\max} , the minimum axial stiffness is calculated by

$$k_z > \frac{mg}{\Delta z_{\max}} \quad (1)$$

where m is the mass of the rotor and its load, and g is the gravitational constant.

The value of the axial stiffness can only be calculated analytically for very specific configurations (e.g., showing practically no leakage flux). In general, it is preferable to predict the value by means of 3-D electromagnetic finite-element method (FEM) simulations or by measurements for the case when a prototype setup is present.

A large axial stiffness also typically goes along with a large tilting stiffness, which is desirable for a stable operation in case of asymmetric forces acting on the rotor, especially for low rotation speeds and standstill (since for high rotation speeds, the gyroscopic effect is additionally stabilizing the rotor).

Enlarging the air gap length δ leads to a decreased axial stiffness (see Fig. 7), and therefore, to increased axial rotor displacements. To still guarantee an adequate axial stiffness, the size of the permanent magnets has to be enlarged for larger air gaps (cf., Fig. 8), whereby it has to be considered that the larger rotor permanent magnets in turn increase the rotor weight.

If an axial deflection due to the load is not acceptable for a certain application, an additional bearing winding varying the premagnetization or a facility to adjust the position of the stator frame is necessary. The tilting error can be eliminated likewise.

Thus, in order to fulfill (1), generally a high axial stiffness is preferable. However, the axial stabilization causes a destabilization in radial direction [12]–[14], which has to be overcome by the stabilizing force of the active radial magnetic bearing. Fig. 9 shows the destabilizing radial force for different air gap lengths. If the rotor is positioned in the geometric center position, the force of the premagnetization is theoretically zero. However,

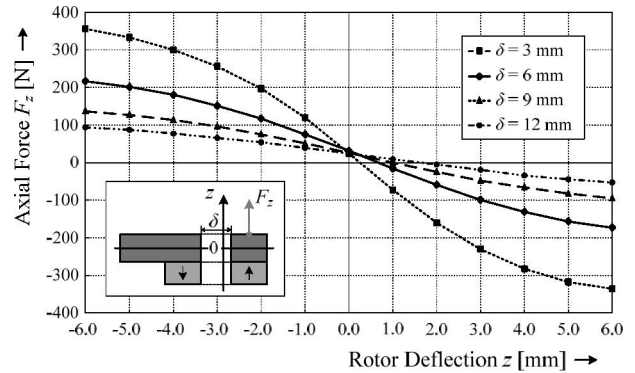


Fig. 7. 3-D FEM simulation results showing the appearing axial force for a rotor deflection in z -direction for different air-gap lengths. The axial stiffness k_z is the gradient of the curves at $z = 0$ mm.

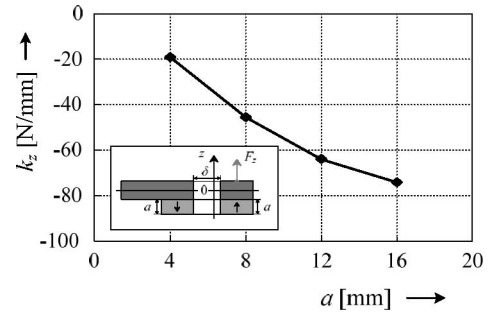


Fig. 8. 3-D FEM simulation results showing the axial stiffness k_z at an air gap length of $\delta = 6$ mm for different heights of the rotor and stator permanent magnets.

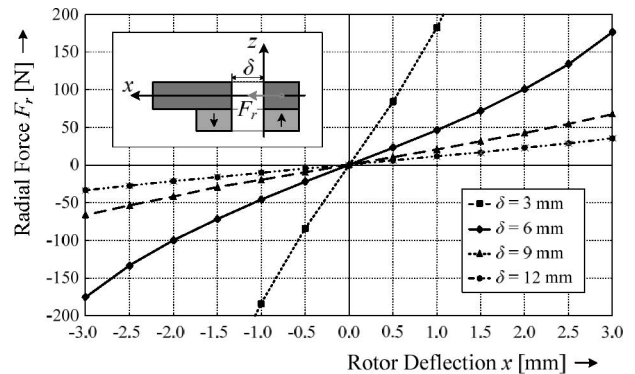


Fig. 9. 3-D FEM simulation results showing the appearing destabilizing radial force for a rotor deflection in x -direction for different air-gap lengths. The radial stiffness k_r is the gradient of the curves at $x = 0$ mm.

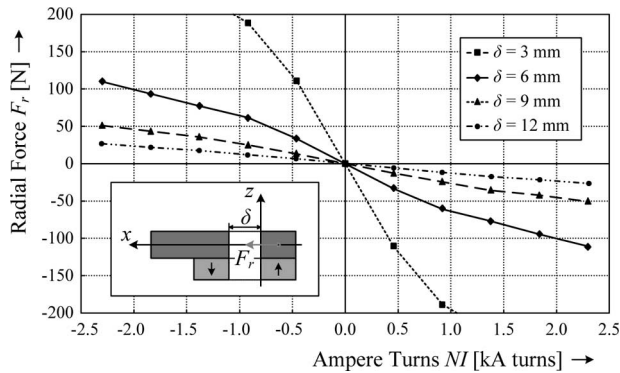


Fig. 10. 3-D FEM simulation results showing the appearing radial force for different air-gap lengths if a bearing current is applied. The force–current factor k_I is the gradient of the curves at $NI = 0$ A turns. For the determination of k_I , the rotor is always kept in the middle.

due to slight asymmetries of the permanent magnets, an additional dc bearing current has to be applied usually in order to maintain the rotor in the geometric middle position.

The radial stiffness k_r (newtons per millimeter) specifies the required force (newton) needed to return the rotor back to its middle position after being radially displaced by 1 mm. By supplying the bearing coils, the flux density in the air gap can be altered depending on the rotor position in order to generate a Maxwell force back toward the target position. This force is described by the force–current factor k_I (newtons per ampere). Therefore, for allowing a maximum radial deflection Δr_{\max} from the target position, the force–current factor has to be larger than a minimum value given by

$$k_I > \frac{k_r \Delta r_{\max}}{N_B I_{B,\max}} \quad (2)$$

where N_B is the bearing coil winding number and $I_{B,\max}$ is the maximum bearing controller current [17]. As the force–displacement dependency is nonlinear, evaluating (2) with a constant radial stiffness k_r is only valid within a small operating range around the target position. The force–current factor can again be calculated by 3-D FEM simulation tools or identified with practical measurements. Fig. 10 shows the 3-D FEM simulation results showing the appearing radial force for different air gap lengths, if a bearing current is applied.

Hence, it seems to be desirable to chose a very high number of bearing turns N_B (for a given maximum allowable bearing current) in order to fulfill (2). However, two limitations have to be considered: First, the assumption of a constant force–current factor k_I is not valid for the case of magnetic saturation. Thus, no significant force increase can be achieved anymore by a higher number of bearing turns and/or current. And second, the number of turns should not be chosen too high in order to avoid instability due to the lowered electrical time constant, as will be shown in the following.

For achieving a stable system control, the fundamental condition

$$\tau_E \ll \tau_M \quad (3)$$

with the mechanical time constant τ_M

$$\tau_M = \sqrt{\frac{m}{k_r}} \quad (4)$$

and the electrical time constant τ_E has to be satisfied obligatorily. The bearing coil has a low-pass filter characteristic with $\tau_E = L_C/R_C$ that usually does not fulfill condition (3). However, the implementation of a subordinate current control loop, as it is usually employed, shifts the control bandwidth to higher frequencies, and consequently, reduces τ_E [18]. The physical limits are then given by the maximum voltage $U_{1,\max}$ applicable to the bearing coils. With this, the electrical time constant τ_E (neglecting the resistance of the bearing coil) is given by

$$\tau_E = \frac{I_{B,\max} L_C}{U_{1,\max}} \quad (5)$$

Since the coil inductance quadratically increases with the number of turns, a compromise between high dynamics (5) with low number of turns and high bearing force (2) with a high number of turns has to be found.

IV. DRIVE DESIGN ASPECTS

For the applications described in the introduction, only a moderate torque is required to overcome the rotor torque resulting from inertia. However, torque requirements arise due to the necessity of a rapid acceleration to ensure a reasonable cycle time of a process. Besides this, a speed range from a few revolutions per minute (for allowing a more homogeneous exposure of a process to the object) up to 1000 r/min or more (spin cycle) must be covered. This leads to a compromise in the choice of the right number of drive poles: a high number of drive poles allows a uniform rotation even at a speed as low as 1 r/min, but leads to a high electrical frequency at higher rotor speeds [see (8)].

In the following, the basic design procedure of the two-phase drive is described. The determination of the proper number of turns of the drive coils is depicted as well as the resulting potential in motor torque and acceleration. The elementary description of the drive design is followed by an optimization procedure focused on the objective to reach a defined rotor speed as quickly as possible while considering the motor controller limitations as dc-link voltage and maximum current capability.

A. Analysis of the Magnetic Circuit

Due to the complex layout of the different lamination stacks and of the permanent magnets resulting in a major ratio of leakage fields, an analytic derivation of the magnetic flux density around the drive lamination stacks is virtually not possible. A 3-D schematic presentation of the main and the leakage fluxes is shown in Fig. 11. However, the magnetic flux density can be calculated by 3-D FEM simulation tools or by measuring the voltage induced in the drive coils. For this measurement, the rotor is driven in single-phase operation and the induced voltage [back electromotive force (EMF)] is measured in the open coils

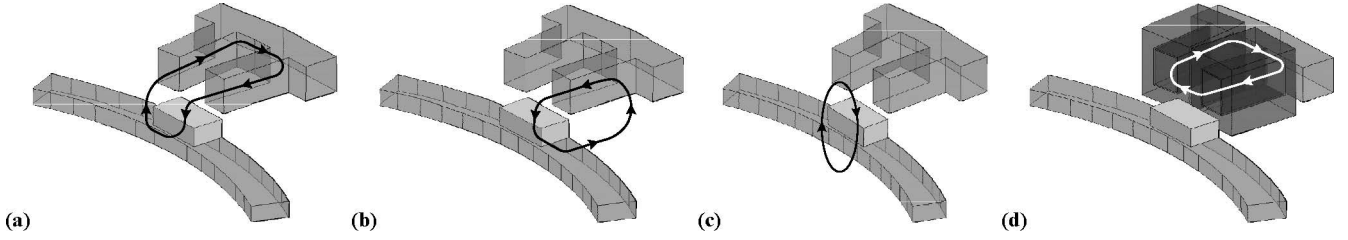


Fig. 11. (a)–(c) 3-D schematic view of the flux lines excited by one permanent magnet on the rotor. About 75% of the flux linked with the drive lamination stack takes the way displayed in (a) and about 25% the way depicted in (b). (c) Possible path of the leakage flux. (d) Because of the big air gap, the flux excited by the bearing coils can also take an undesired shortened way, especially if the distance between both legs of the drive lamination stack is smaller than the air-gap length.

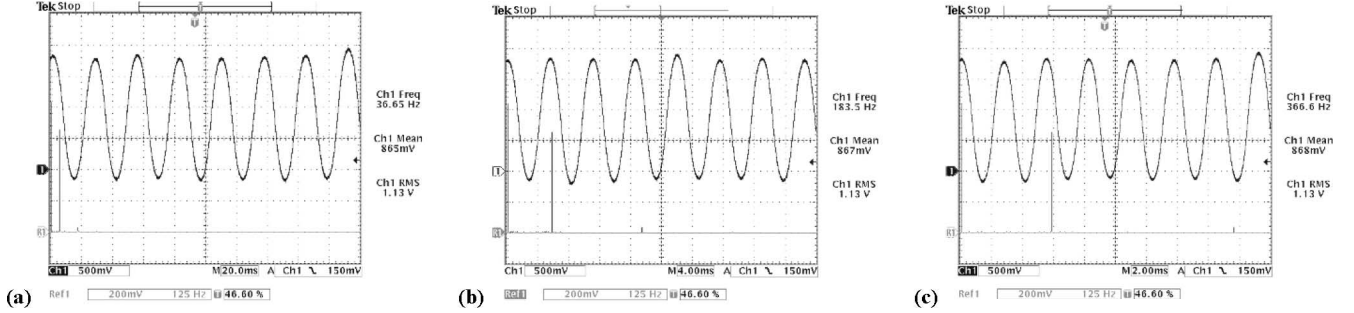


Fig. 12. Magnetic flux density B measured with a tesla meter in the central point of a drive lamination stack (Ch1: 10 mV = 1 mT) and its spectrum analysis (ChR1) for (a) 100 r/min ($f_{el} = 36.7$ Hz), (b) 500 r/min ($f_{el} = 183.3$ Hz), and (c) 1000 r/min ($f_{el} = 366.7$ Hz). The time-dependent behavior of $B(t)$ is sinusoidal, and its amplitude is speed-independent of the rotor speed.

of the second phase. The induced voltage $U_{ind}(t)$ can be derived as

$$\begin{aligned} u_{ind}(t) &= kN \frac{d\phi}{dt} = kN \left(A \frac{dB}{dt} + B \frac{dA}{dt} \right) \\ &= kNA \frac{dB}{dt} \end{aligned} \quad (6)$$

where k is the number of drive coils per drive phase, N the number of turns of one drive coil, A the cross-sectional area of the drive lamination stack, and B the magnetic flux density in the core. As will be shown later, the induced voltage and its scaling with rotation speed and number of turns is one crucial parameter in the optimization procedure of the drive. Thus, these dependencies will be derived from (6) in the following.

Fig. 12 shows the magnetic flux density B measured with a tesla meter in the central point of a drive lamination stack at different rotor speeds n_R . Due to the arrangement of the permanent magnets, B has a nonzero average, but its amplitudes are independent of the rotor speed. The crucial factor for the induced voltage and the motor torque, respectively, is just the alternating (sinusoidal) component of B , since the dc part does not affect any force. As a result of the large leakage fields, the magnetic flux density B is not homogeneously distributed over the entire pole face. Thus, dividing the measured value $u_{ind}(t)$ by kNA leads to an average value of dB/dt over the entire pole face.

The time-dependent behavior of $B(t)$ is virtually sinusoidal as a spectrum analysis of $B(t)$ shows in Fig. 12, and can, therefore, be written as

$$B(t) = B_0 + \hat{B} \sin(\omega_{el}t). \quad (7)$$

TABLE II
RMS VALUE OF THE INDUCED VOLTAGE U_{ind} AND kU_{ind} MEASURED IN THE EXPERIMENTAL SETUP ($p = 22$) IN ONE DRIVE COIL ($N = 300$) FOR DIFFERENT ROTOR SPEEDS n_R

n_R [r/min]	f_{el} [Hz]	U_{ind} [V]	kU_{ind} [mV/(r/min)]
200	73.3	2.2	11.0
400	146.7	4.1	10.3
600	220.0	6.0	9.9
800	293.3	7.9	9.8
1000	366.7	9.8	9.8
1200	440.0	11.8	9.8

The frequency ω_{el} of the induced voltage $u_{ind}(t)$ is calculated from the rotor speed n_R (in revolutions per minute) and the number of pole pairs p of the rotor

$$\omega_{el} = 2\pi f_{el} = 2\pi \frac{n_R}{60} p. \quad (8)$$

From this, the induced voltage can be derived with (6)–(8) as

$$u_{ind}(t) = k2\pi \frac{n_R}{60} pN \hat{B} A \cos\left(2\pi \frac{n_R}{60} pt\right). \quad (9)$$

The rms value U_{ind} of $u_{ind}(t)$ follows to

$$U_{ind} = k2\pi \frac{n_R}{60} pN \frac{\hat{B}}{\sqrt{2}} A. \quad (10)$$

Table II shows the values of the induced voltage measured in the experimental setup. Due to the proportionality of U_{ind} and the rotor speed n_R , a speed-independent and almost constant factor kU_{ind} per drive coil can be assessed for a certain winding number N_0 by averaging the induced voltages of different

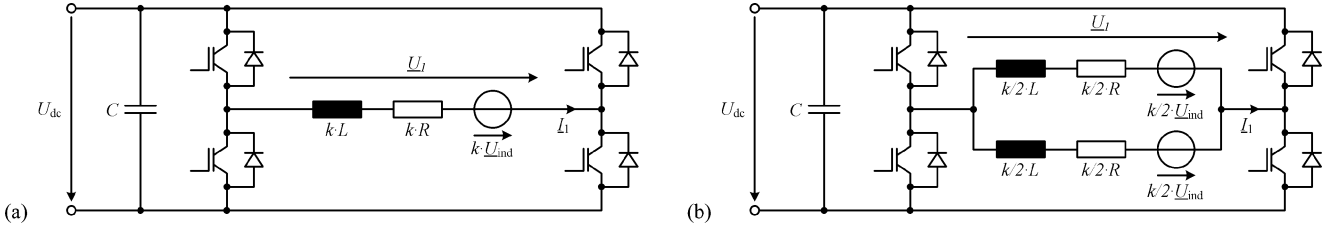


Fig. 13. Equivalent electrical circuit of one drive phase with k drive coils. (a) Connected in series. (b) Connected in parallel.

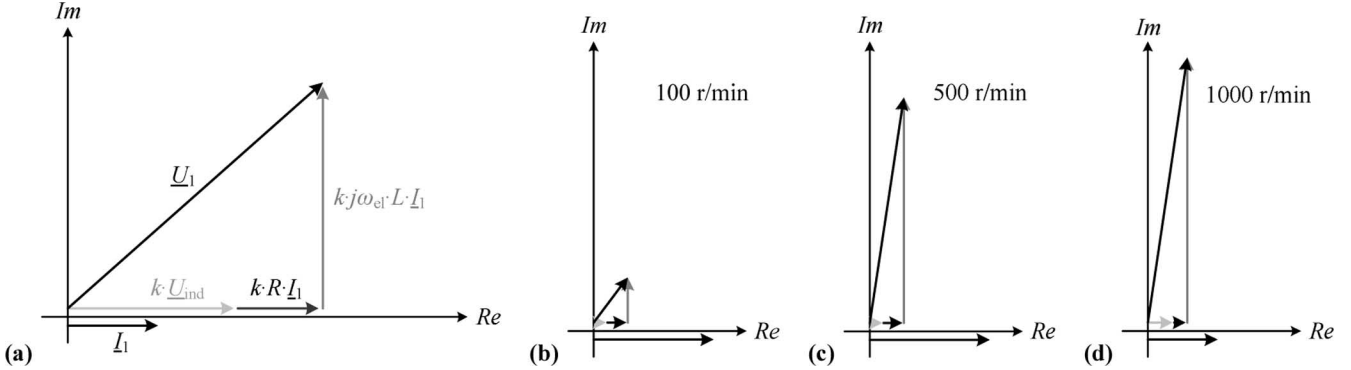


Fig. 14. (a) Phasor chart of the equivalent electrical circuit of one drive phase with the basic phasor orientation. Calculated phasor charts for $N_1 = N_0 = 300$ and $k = 2$ for a motor controller with a dc-link voltage of $U_{dc} = 325$ V ($U_1 = 218$ V) and a drive current limit of $I_{1,max} = 14.1$ A for a rotor speed of (b) 100 r/min, (c) 500 r/min, and (d) 1000 r/min within each case the maximal possible drive current I_1 and the maximal motor torque, respectively.

rotation speeds according to

$$kU_{ind}(N_0) = \frac{1}{i} \sum \frac{U_{ind,i}(N_0)}{kn_{R,i}} \approx \frac{2\pi}{60} p N_0 \frac{\hat{B}}{\sqrt{2}} A. \quad (11)$$

In reality, eddy-current effects slightly decrease kU_{ind} for higher frequencies, wherefore, the averaged value of kU_{ind} in (11) is only an approximation (also see Table II). With this, the linear dependency of the induced voltage on the rotation speed and the number of turns can be expressed by

$$U_{ind} = kU_{ind}(N_0) n_R \frac{N_1}{N_0} \quad (12)$$

where N_1 is tentatively optimized and N_0 is the initial number of turns.

B. Equivalent Electrical Circuit of One-Drive Phase

The equivalent electrical circuit consists of the aforementioned derived induced voltage U_{ind} , of the coil resistance R , the coil inductivity L , and of the voltage source U_1 . Typically, the drive coils are placed within the two legs of an H-bridge and $u_1(t)$ is described by

$$u_1(t) = \gamma U_{dc} \sin(\omega_{el} t + \varphi) \quad (13)$$

where U_{dc} is the dc-link voltage, γ is the duty cycle of the H-bridge (with a typical maximum of about 95%), and φ the phase angle between U_1 and I_1 . Hence, the rms value U_1 of $u_1(t)$ is calculated by

$$U_1 = \frac{\gamma U_{dc}}{\sqrt{2}}. \quad (14)$$

Advantageously, all of the k drive coils are connected in series, as shown in Fig. 13(a). Even though there are also alternative

connections possible, e.g., half of them in parallel, as depicted in Fig. 13(b), all possibilities result in the same maximum torque. As a detailed analysis shows, the number of turns has to be adapted, while the current density in the coils stays constant. Thus, the following considerations are based on the series connection. Applying Kirchhoff's law to the equivalent electrical circuit for the configuration with drive coils in series connection leads to

$$U_1 = kR I_1 + k j \omega_{el} L I_1 + k U_{ind} \quad (15)$$

or for the second configuration, respectively, to

$$U_1 = \frac{k}{2} R \frac{I_1}{2} + \frac{k}{2} j \omega_{el} L \frac{I_1}{2} + \frac{k}{2} U_{ind}. \quad (16)$$

The following calculations are carried out corresponding to the first configuration with serial connection of all coils. The induced voltage is due to the field-orientated control in phase with the drive current I_1 , and together with the phasor chart [see Fig. 14(a)], the following equation can be derived:

$$(kU_{ind} + kR I_1)^2 + (\omega_{el} k L I_1)^2 = U_1^2. \quad (17)$$

From this, the drive current I_1 is computed with

$$I_1 = \frac{-U_{ind} R \pm \sqrt{(R^2 + \omega_{el}^2 L^2) \frac{U_1^2}{k^2} - \omega_{el}^2 L^2 U_{ind}^2}}{R^2 + \omega_{el}^2 L^2}. \quad (18)$$

The resistance R of one coil is calculated by applying

$$R = \rho(1 + \alpha_{T_0}(T - T_0)) \frac{Nl}{(d/2)^2 \pi} \quad (19)$$

where ρ is the resistivity, α_{T_0} the temperature coefficient at T_0 (e.g., 20°C), T the operating temperature (e.g., 75°C), N the number of turns, l the average length of one turn, and d the

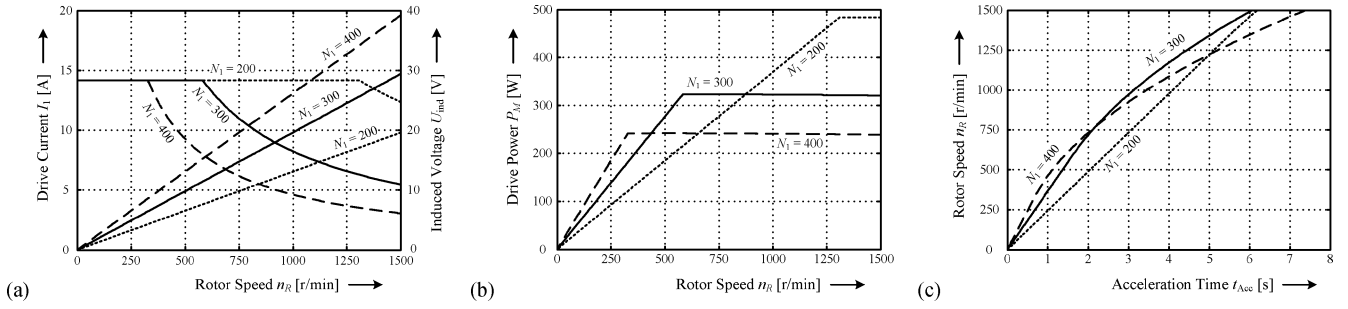


Fig. 15. Calculated characteristics for a dc-link voltage of $U_{dc} = 325$ V and a drive current limit of $I_{1,max} = 14.1$ A. (a) Current and induced voltage of one drive phase. (b) Drive power (of two drive phases) as a function of the rotor speed n_R . (c) Acceleration capability of the motor.

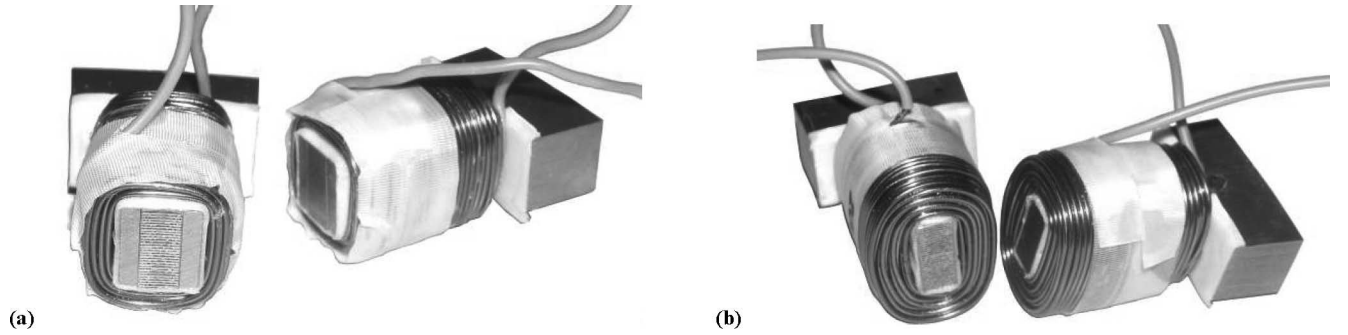


Fig. 16. Drive coil segments with (a) a big iron cross section for an increased motor torque and (b) with a small inductivity for a good acceleration capability in the higher speed range.

wire diameter. If R_0 is the resistivity of a drive coil with N_0 number of turns, the resistivity R_1 at N_1 number of turns is approximated by

$$R_1 \approx \frac{N_1}{N_0} R_0. \quad (20)$$

The inductivity L of the U-shaped drive coils (cf., Fig. 5) cannot be ascertained by analytical formulas due to the large air gap and the dominance of leakage field effects in this configuration. Therefore, measurements and/or 3-D FEM electromagnetic simulations again provide an initial inductance value L_0 for a certain initial turns number N_0 . The actual inductance L_1 for a specific turns number N_1 is then given by the scaling law

$$L_1 \approx \frac{N_1^2}{N_0^2} L_0. \quad (21)$$

Now, the phasor charts and the behavior of U_{ind} and I_1 can be calculated in dependency of the rotation speed for different numbers of turns. The current limit $I_{1,max}$ and the maximum output voltage $U_{1,max}$ given by the motor controller specifications can also be taken into consideration for the selection of the optimum number of drive turns. Fig. 14(b)–(d) shows exemplarily the phasor charts for $N_1 = N_0 = 300$ and $k = 2$ for the motor parameters given in Section V, and for a motor controller with a dc-link voltage of $U_{dc} = 325$ V and the rms drive current I_1 limited to a maximum of $I_{1,max} = 14.1$ A. The phasor diagrams illustrate that due to the big air gap the induced voltage is comparatively low and the motor shows mainly inductive behavior. Fig. 15(a) depicts the dependency of U_{ind} and I_1 on the rotor speed varying the number of turns N_1 .

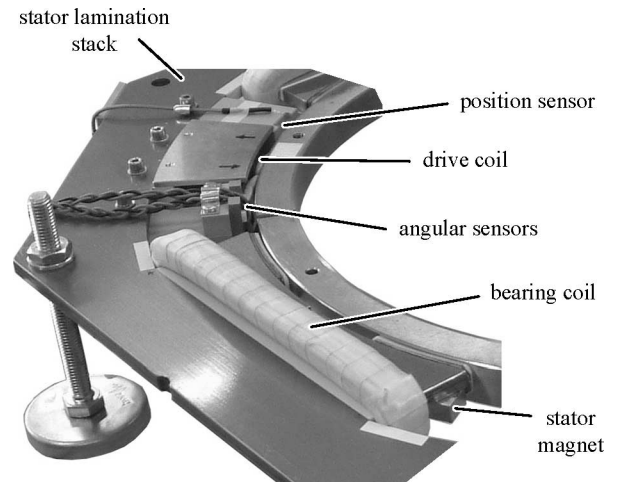


Fig. 17. Detailed view of the experimental setup with the motor stator and its components.

C. Motor Power and Acceleration

The motor drive power P_M of one phase can be calculated on the one hand by

$$P_M = M_M 2\pi \frac{n_R}{60} \quad (22)$$

and on the other hand, for the case of field-oriented control and the assumption of sinusoidal currents, and no occurrence of saturation effects in the drive lamination stacks by

$$P_M = mkU_{ind}I_1 = mk \frac{N_1}{N_0} kU_{ind}(N_0)n_R I_1 \quad (23)$$

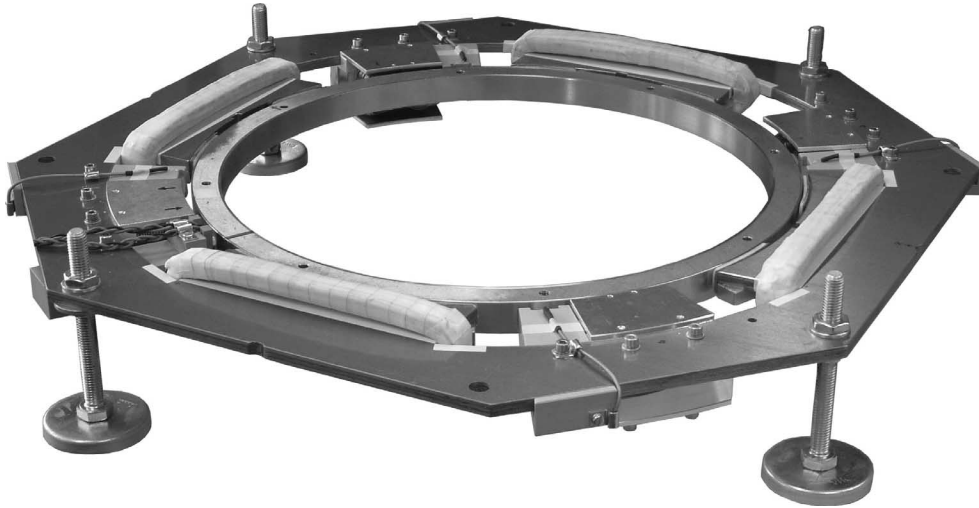


Fig. 18. Experimental setup with an inside rotor diameter of 410 mm and a mechanical air gap of 5 mm.

where m is the number of drive poles. Combining (22) and (23), the motor torque is directly proportional to the drive current I_1

$$M_M = m \frac{60k}{2\pi} \frac{N_1}{N_0} k_{U_{\text{ind}}}(N_0) I_1 \quad (24)$$

and therefore, constant as long as $I_1 = I_{1,\text{max}}$ [cf., Fig. 15(b)].

The rotor acceleration capability is derived from the energy, which is fed to the rotor within an infinitesimal time step dt

$$dE = P_M dt = mk \frac{N_1}{N_0} k_{U_{\text{ind}}}(N_0) n_R I_1 dt \quad (25)$$

leading to an acceleration of the rotor, and therefore, to an increased rotatory energy

$$E = \frac{1}{2} J \omega_R^2 \quad (26)$$

where J is the rotor moment of inertia in the direction of the rotation axis. Equation (26) can be transformed into

$$dE = J \left(\frac{2\pi}{60} \right)^2 n_R dn_R \quad (27)$$

and finally, together with (25), the necessary acceleration time t_{Acc} that the rotor needs to reach a desired process speed n_P can be computed with

$$t_{\text{Acc}} = \frac{J}{mk k_{U_{\text{ind}}}(N_0)} \left(\frac{2\pi}{60} \right)^2 \frac{N_0}{N_1} \int_0^{n_P} \frac{1}{I_1(n_R)} dn_R. \quad (28)$$

Fig. 15(c) depicts the calculated values for the acceleration time for reaching different rotation speeds depending on the number of turns of the drive coils.

D. Optimization of the Number of Coil Turns

The calculated characteristics depicted in Fig. 15 illustrate the behavior of the drive depending on the number of turns of the drive coils: a large number of turns increase the induced voltage, and therefore, the delivered power for acceleration. However, the large inductance arising from the increased turns

number combined with the high number of poles [resulting in high electrical frequency, cf., (8)] generates a large inductive voltage drop reducing the maximum possible drive current even at a comparatively low speed. Therefore, the reactive power is large compared to the effective power, which is obviously a result of the weak magnetic coupling due to the large width of the air gap.

Thus, the drive design requires a compromise between a large induced voltage (high number of turns) and a small inductance (small number of turns) for a specific required maximum rotational speed. Therefore, an optimization with respect to the maximum achievable acceleration leads to a moderate torque in the low-speed range.

Besides this, the behavior of the drive is affected by the design of the drive coil lamination stack. A coil with a rather big iron cross section [Fig. 16(a)] generates a higher motor torque (due to higher induced voltage) for smaller ampere-turns, and is therefore preferable for applications, where high torque in the low-speed range is required. On the other hand, a coil with a small iron cross section [Fig. 16(b)] leads to a small coil inductivity, and therefore, allows a good acceleration capability in the higher speed range, but the iron core shows increased saturation tendencies (transformer lamination stacks M270-50A have been used), which may degrade the torque, especially in the low-speed region, where higher currents occur.

For bearingless motors with large air gaps, a drive claw design without any expanded pole shoes improves the field flux linkage with the rotor magnets, as the magnetic resistance of the air gap remains smaller than the magnetic resistance of the claw gap [19], [20].

V. EXPERIMENTAL PERFORMANCE

A first prototype of the proposed hollow-shaft motor has been realized (cf., Figs. 17 and 18, and its key data in Table III) and its rotor acceleration time from 0 to 1250 r/min has been optimized according to the guidelines given in the previous section

TABLE III
KEY DATA OF THE EXPERIMENTAL SETUP

Inside rotor diameter	410 mm
Magnetic air gap	6 mm
Mechanical air gap	5 mm
Maximum torque	4.5 Nm
Maximum axial load	160 N
Axial stiffness k_z	-45.5 N/mm
Tilting stiffness k_ϕ	-59.5 Nm/°
Number of pole pairs p	22
Number of bearing phases	2
Number of bearing coils per phase	2
Number of drive phases m	2
Number of drive coils per phase k	2
Maximal speed $n_{R,max}$	1250 r/min
Drive coil resistance R_0 ($N_0 = 300$)	0.55 Ω
Drive coil inductivity L_0 ($N_0 = 300$)	5.7 mH
Induced voltage factor per drive coil $k_{U,ind}$ ($N_0 = 300$)	9.8 mV/(r/min)

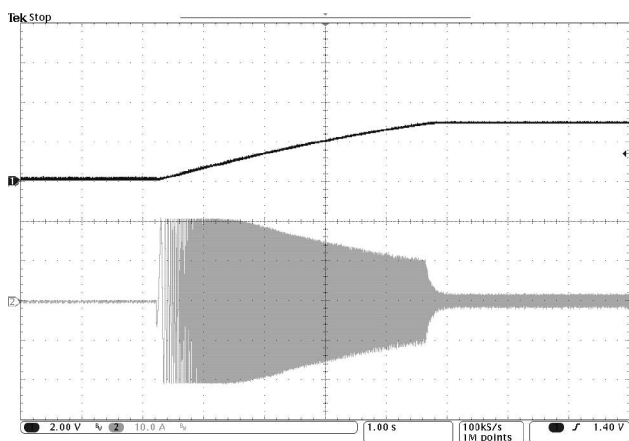


Fig. 19. Acceleration behavior of the experimental setup from 0 to 1250 r/min (Ch1: n_R , 800 r/min/div) for $N_1 = 300$ and a maximum drive current of $I_{1,pp} = 40$ A (Ch2: I_1 , 10 A/div).

(cf., Fig. 19). It can be seen that the maximal achievable drive current decreases due to the large inductance of the drive coils for higher rotor speeds, as calculated in Fig. 15(a). Starting from a current peak-to-peak value of $I_{1,pp} = 40$ A (which corresponds to an rms value of $I_1 = 14.1$ A), the drive current is approximately halved as soon as the desired speed of 1250 r/min is reached.

VI. CONCLUSION

This paper describes a novel and compact concept for contactless levitation and rotation of an annular rotor through the walls of a process chamber. In the proposed setup, a homopolar magnetic bearing biased by permanent magnets is combined with a high-pole-number segment motor.

In this paper, guidelines for the design of the bearing part, and for the design and optimization of the drive part of the system have been presented. The large width of the air gap and the drive configuration result in a weak magnetic coupling of rotor and

stator. Thus, the drive design requires a compromise between a large induced voltage and a small number of turns of the drive coils; on the one hand, a large inductance combined with a high number of poles resulting in high electrical frequency leads to a major inductive voltage drop, thus reducing the maximum possible drive current at a comparatively low rotor speed, but allows for a high torque in the low-speed range. On the other hand, an optimization with respect to a reasonable achievable acceleration in the high-speed range leads to a moderate torque in the low-speed range due to the small number of coil turns.

Due to its compact and lightweight construction, its high axial and tilting stiffness, and its good acceleration capability, the proposed bearingless hollow-shaft motor is highly suitable for the treatment of process objects within a hermetically closed process chamber in ultraclean applications, such as biotechnology and semiconductors. The employment of the new concept in these applications may represent a step toward significant improvement in terms of controlling process conditions and purity.

REFERENCES

- [1] M. Quirk and J. Serda, *Semiconductor Manufacturing Technology*. Englewood Cliffs, NJ: Prentice-Hall, 2000.
- [2] T. Schneeberger and J. W. Kolar, "Novel integrated bearingless hollow-shaft drive," in *Proc. 2006 IEEE Int. Conf. Ind. Appl.*, Tampa, FL, Oct., vol. 1, pp. 70–75.
- [3] R. Schöb, N. Barletta, M. Weber, and R. von Rohr, "Design of a bearingless bubble bed reactor," in *Proc. 6th Int. Symp. Magn. Bearings*, Cambridge, MA, 1998, pp. 507–516.
- [4] W. Gruber and A. Amrhein, "Design of a bearingless segment motor," presented at the 10th Int. Symp. Magn. Bearings, Martigny, Switzerland, 2006.
- [5] S. Silber, W. Amrhein, P. Bösch, R. Schöb, and N. Barletta, "Design aspects of bearingless slice motors," *IEEE/ASME Trans. Mechatronics*, vol. 10, no. 6, pp. 611–617, Dec. 2005.
- [6] P. Bösch and N. Barletta, "High power bearingless slice motor (3–4 kW) for bearingless canned pumps," presented at the 9th Int. Symp. Magn. Bearings, Lexington, KY, 2004.
- [7] T. Ohishi, Y. Okada, and K. Dejima, "Analysis and design of a concentrated wound stator for synchronous-type levitated rotor," in *Proc. 4th Int. Symp. Magn. Bearings*, Zürich, Switzerland, 1994, pp. 201–206.
- [8] A. Chiba, D. T. Power, and M. A. Rahman, "Characteristics of a bearingless induction motor," *IEEE Trans. Magn.*, vol. 27, no. 6, pp. 5199–5201, Nov. 1991.
- [9] R. Schöb and J. Bichsel, "Vector control of the bearingless motor," in *Proc. 4th Int. Symp. Magn. Bearings*, Zürich, Switzerland, 1994, pp. 327–332.
- [10] M. Ooshima, A. Chiba, T. Fukao, and M. A. Rahman, "Design and analysis of permanent magnet-type bearingless motors," *IEEE Trans. Ind. Electron.*, vol. 43, no. 2, pp. 292–299, Apr. 1996.
- [11] N. Barletta and R. Schöb, "Design of a bearingless blood pump," presented at the 3rd Int. Symp. Magn. Suspension Technol., Tallahassee, FL, 1995.
- [12] J.-P. Yonnet, "Permanent magnet bearings and couplings," *IEEE Trans. Magn.*, vol. 17, no. 1, pp. 1169–1173, Jan. 1981.
- [13] S. Earnshaw, "On the nature of the molecular forces which regulate the constitution of the luminiferous ether," *Trans. Cambridge Philos. Soc.*, vol. 7, pp. 97–112, 1839.
- [14] J. Delamare, E. Rulliere, and J. P. Yonnet, "Classification and synthesis of permanent magnet bearing configurations," *IEEE Trans. Magn.*, vol. 31, no. 6, pp. 4190–4192, Nov. 1995.
- [15] G. Schweizer, H. Bleuler, and A. Traxler, *Active Magnetic Bearings*. Berlin, Germany: Springer-Verlag, 1993.
- [16] J. Zhang, J. O. Schulze, and N. Barletta, "Synchronous three-level PWM power amplifier for active magnetic bearings," in *Proc. 5th Int. Symp. Magn. Bearings*, Kanazawa, Japan, 1996, pp. 277–282.
- [17] P. Karutz, T. Nussbaumer, W. Gruber, and J. W. Kolar, "Novel magnetically levitated two-level motor," *IEEE/ASME Trans. Mechatronics*, vol. 13, no. 6, pp. 658–668, Dec. 2008.
- [18] A. Chiba, T. Fukao, O. Ichikawa, M. Ooshima, M. Takemoto, and D. Dorrell, *Magnetic Bearings and Bearingless Drives*. Boston, MA: Newnes, 2005.

- [19] Y. Pang, Z. Q. Zhu, and D. Howe, "Analytical determination of optimal split ratio for permanent magnet brushless motors," *Proc. Inst. Electr. Eng.—Electr. Power Appl.*, vol. 153, no. 1, pp. 7–13, 2006.
- [20] P. Karutz, T. Nussbaumer, W. Gruber, and J. W. Kolar, "Saturation effects in high acceleration bearingless slice motors," in *Proc. IEEE Int. Symp. Ind. Electron.*, Cambridge, U.K., Jul. 2008, pp. 472–477.



Thomas Schneeberger (S'06) was born in Olten, Switzerland, in 1977. He received the M.Sc. degree in electrical engineering from the Swiss Federal Institute of Technology (ETH) Zürich, Zürich, Switzerland, in 2003, and the Ph.D. degree from the Power Electronic Systems Laboratory, ETH Zürich, in 2009.

Since March 2009, he has been with Levitronix GmbH, Zürich, Switzerland, where he is currently engaged in magnetically levitated spin drives for the semiconductor process industry. His current research interests include electric drive systems, particularly magnetically levitated motors, and power electronics.



Thomas Nussbaumer (S'02–M'06) was born in Vienna, Austria, in 1975. He received the M.Sc. degree (with honors) in electrical engineering from the University of Technology Vienna, Vienna, Austria, in 2001, and the Ph.D. degree from the Power Electronic Systems (PES) Laboratory, Swiss Federal Institute of Technology (ETH) Zürich, Zürich, Switzerland, in 2004.

From 2001 to 2006, he was with the PES, where he conducted research on the modeling design, control, and modulation of three-phase rectifiers, power factor correction techniques, and electromagnetic compatibility. Since 2006, he has also been with Levitronix GmbH, Zürich, Switzerland, where he is currently working on permanent-magnet motor drives, and magnetic levitation for the semiconductor and biotechnology industry.



Johann W. Kolar (M'89–SM'04) received the Ph.D. degree (*summa cum laude/promotio sub auspiciis praesidentis rei publicae*) from the University of Technology Vienna, Vienna, Austria.

Since 1984, he has been an Independent International Consultant in close collaboration with the University of Technology Vienna, and is engaged in the fields of power electronics, industrial electronics, and high-performance drives. Since February 1, 2001, he has been a Professor and the Head of the Power Electronic Systems Laboratory, Swiss Federal Institute of Technology (ETH) Zürich, Zürich, Switzerland. He has proposed numerous novel pulsewidth modulation (PWM) converter topologies, and modulation and control concepts, e.g., the VIENNA rectifier and the three-phase ac–ac sparse matrix converter. He has authored or coauthored more than 250 scientific papers published in international journals and conference proceedings, and has filed more than 70 patents. Since 2002, he has been an Associate Editor of the *Journal of Power Electronics* of the Korean Institute of Power Electronics and a member of the Editorial Advisory Board of the *Institute of Electrical Engineers of Japan (IEEJ) Transactions on Electrical and Electronic Engineering*. His current research interests include ac–ac and ac–dc converter topologies with low effects on the mains, e.g., for power supply of telecommunication systems, more-electric aircraft and distributed power systems in connection with fuel cells, the realization of ultracompact intelligent converter modules employing the latest power semiconductor (SiC) technology, novel concepts for cooling and electromagnetic interference (EMI) filtering, multidomain/multiscale modeling and simulation, pulsed power, bearingless motors, and power microelectromechanical system (MEMS).

Prof. Kolar is a member of the IEEJ and the Technical Program Committees of numerous international conferences in the field (e.g., he is the Director of the Power Quality Branch of the International Conference on Power Conversion and Intelligent Motion). From 1997 to 2000, he was an Associate Editor of the IEEE TRANSACTIONS ON INDUSTRIAL ELECTRONICS. Since 2001, he has been an Associate Editor of the IEEE TRANSACTIONS ON POWER ELECTRONICS. He received the Best Transactions Paper Award from the IEEE Industrial Electronics Society in 2005 and an Erskine Fellowship from the University of Canterbury, New Zealand, in 2003.